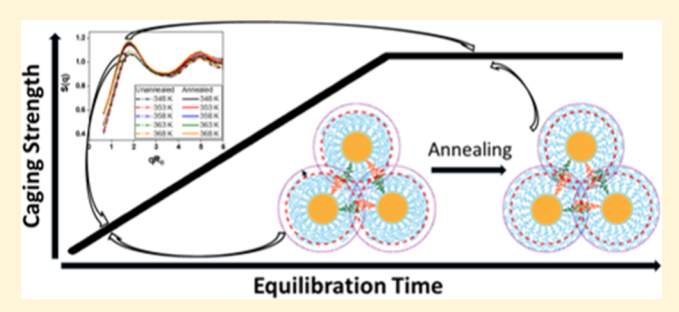
Macromolecules XXXX, XXX, XXX-XXX

Microscopic Origins of Caging and Equilibration of Self-Suspended **Hairy Nanoparticles**

Xiaotun Liu, Brooks A. Abel, Qing Zhao, Shuke Li, Snehashis Choudhury, Jingxu Zheng, and Lynden A. Archer

Supporting Information

ABSTRACT: Well-dispersed, solvent-free silica nanoparticles tethered with polymers exhibit soft glassy rheology and jamming behavior because of the cages induced by interpenetrated chains. In this study, we use small-angle X-ray scattering and rheology to investigate slow structural and mechanical evolution of a soft glassy material composed of silica nanoparticles densely grafted with poly(ethylene glycol) methyl ether (mPEG) chains. We observe a significant equilibration process that has not been reported previously and show that the process is thermally activated and associated with local rearrangements of tethered chains to



their equilibrium conformations. At a fixed temperature, the strength of the equilibrated cages increases significantly, relative to their unequilibrated values, but decreases in a predictable manner as the temperature rises. A simple geometrical model is used to rationalize these observations in terms of corona interpenetration, cage dynamics, and yielding of self-suspended nanoparticles.

INTRODUCTION

Over the past few decades, soft glassy materials such as colloidal suspensions, emulsions, and star polymers have gathered considerable attention. Exhibiting a distinct yield stress and jamming behavior, these materials are of interest both from a scientific perspective, as model material systems for studying suspension stability, 1-12 and from a practical viewpoint for their wide applications in advanced coatings, energy storage, thixotropic materials, and biomedical engineering. 13-22 The self-suspended hairy nanoparticles of interest in this study are a subset of this broader class of materials and consist of nanoparticles that are ionically or covalently tethered with polymer chains. ^{23–30} At high grafting densities of moderate molecular weight polymer chains, the tethered polymer serves as the suspending medium, and the systems are intrinsically well-dispersed. Compared to other soft glassy materials, the self-suspended hairy nanoparticles possess other important features. First, the solventless nature of the materials allows for study of interparticle interactions without the complication of enthalpic effects with solvents. Second, because the solvent is covalently attached, its vapor pressure is essentially zero up to the thermal decomposition temperature. This makes the study of long-time thermal behaviors possible without concerns about solvent loss that limits detailed thermal aging studies for other soft-glassy materials. In addition, because the chains are all confined to and between the nanoparticle cores, the systems provide a straightforward tool for interrogating interfacial physics of the tethered chains

through bulk measurements. Recently, hairy nanoparticles and their derivatives in which ion-conducting oligomers or ionic liquids tethered to the particle cores have also found applications as solid-state electrolytes and membrane separators in batteries, 31,32 which has increased a fundamental interest in understanding transport processes in the materials.

Previous studies have shown that the nanoparticle core size, grafting density, and polymer molecular weight play synergistic roles in determining the material properties. The viscosity of the materials have been reported to diverge at particle volume fractions well below those normally required for conventional suspensions to jam or crystallize.³³ This finding implies that some fraction of the tethered polymer behaves dynamically as part of the cores.²⁴ Likewise, glassy and jamming behavior is enhanced in SiO₂-PEG/SiO₂-PMMA self-suspended hairy nanoparticle mixtures in which the Flory-Huggins interaction parameter (χ) for the corona chains is negative. ²⁴ On the other hand, there are reports that these behaviors can be completely lost at sufficiently low core volume fractions where the ligand interpenetration and overlap are limited.²³ From a microscopic perspective, the packing of spherical nanoparticle cores inevitably creates an interstitial space that the tethered chains need to fill to satisfy the uniform density constraint. This process by itself would lead to more interdigitated chains and

Received: July 15, 2019 Revised: September 9, 2019

[†]Robert Frederick Smith School of Chemical and Biomolecular Engineering, [‡]Department of Chemistry and Chemical Biology, and [§]Department of Materials Science and Engineering, Cornell University, Ithaca, New York 14853, United States

$$(EtO)_3Si \longrightarrow NCO + HO \longrightarrow \bigcap_n \xrightarrow{DABCO} \xrightarrow{CH_2Cl_2, 50 \text{ °C}, 48 \text{ h}} (EtO)_3Si \longrightarrow \bigcap_n \xrightarrow{N} O \longrightarrow \bigcap_n O$$

Figure 1. Synthesis of PEG-tethered silica nanoparticles.

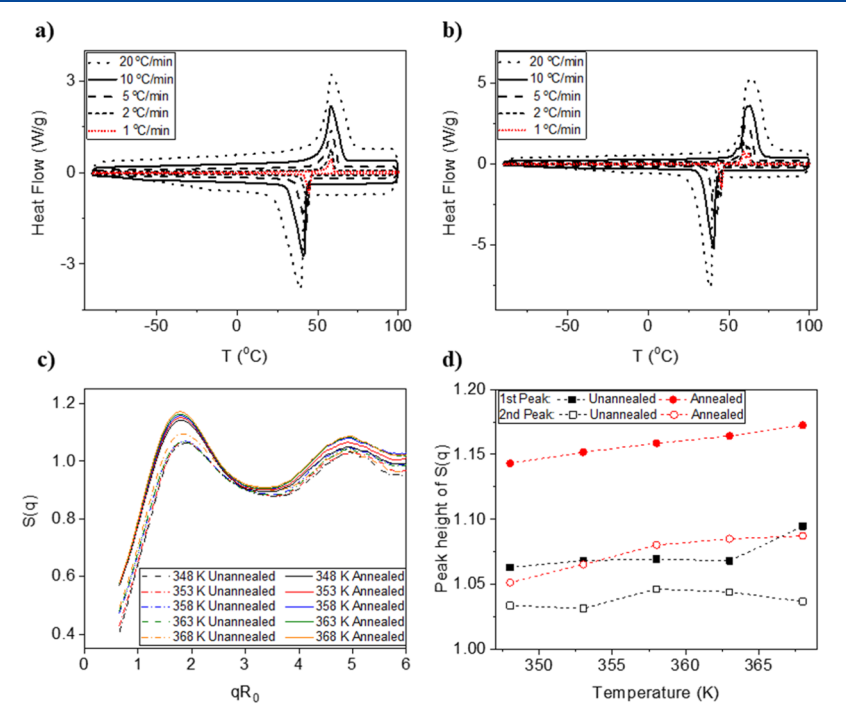


Figure 2. Heat flow as a function of temperature at various ramping rates for (a) self-suspended hairy nanoparticles and (b) neat mPEG-OH. (c) Structure factor S(q) of unannealed and annealed hairy nanoparticles as a function of normalized wave vector qR_0 at various temperatures (d) first and second peak heights of S(q) for the unannealed and annealed materials as a function of temperature. R_0 is the average radius of the nanoparticle cores and $R_0 \approx 5$ nm.

caging processes that hinder the dynamics of the chains and associated particles. 25,28,34

In this study, we consider for the first time how caging evolves in a self-suspended nanoparticle fluid. We first drive the systems out of equilibrium and interrogate their structural evolution toward equilibrium using small-angle X-ray scattering (SAXS) and rheological analysis. This work provides insights into the microscopic origins of cage formation and how nanoparticle cages develop and evolve in self-suspended materials. We take advantage of these insights to evaluate a simple microscopic model for yielding that helps to explain the temperature dependence of the cage strength and the role that the core volume fraction plays in setting material properties.

EXPERIMENTAL METHODS

Materials. Silica nanoparticles (LUDOX SM30, 10 \pm 2 nm), poly(ethylene glycol) monomethyl ether (mPEG–OH) with $M_{\rm n}=5000~{\rm Da}, 3$ -(triethoxysilyl)propyl isocyanate, 1,4-diazabicyclo [2.2.2.]-octane (DABCO), and anhydrous dichloromethane were purchased from Sigma-Aldrich. The mPEG–OH was dried in vacuo overnight at room temperature before use. All other reagents were used as received.

The synthesis of PEG-tethered silica nanoparticles is illustrated in Figure 1. A mixture of mPEG-OH ($M_n = 5000 \text{ Da}$) (10.0 g, 2.00 mmol, 1.00 equiv), 3-(triethoxysilyl)propyl isocyanate (0.495 g, 2.00 mmol, 1.00 equiv), and DABCO (0.336 g, 3.00 mmol, 1.50 equiv) was prepared in anhydrous dichloromethane (10 mL) and heated to 50 °C for 48 h. The reaction mixture was precipitated into excess hexanes and the mPEG-silane product was isolated by vacuum filtration, dried in vacuo at room temperature, and stored at 2-8 °C prior to use. Silica nanoparticles (LUDOX SM30, 10 ± 2 nm) (0.430 g) were reacted with the triethoxysilane-functional mPEG product (4.00 g) from the previous step in deionized water (120 mL) under argon atmosphere at 70 °C for 48 h. The resultant polymer-tethered silica nanoparticles were isolated by lyophilization and further purified by repeated precipitation into a 1:4 (v/v) mixture of chloroform/ hexanes, followed by centrifugation at 8500 rpm. The resultant material was dried thoroughly in a vacuum oven before storage under

Thermal Analysis of PEG-Tethered Silica Nanoparticles. The inorganic content of the polymer-tethered silica nanoparticles was estimated from thermogravimetric analysis (TGA) using a TA Instruments Q500 thermogravimetric analyzer. TGA was performed under a nitrogen atmosphere from 20 to 600 °C at 10 °C/min. The results show that under the current synthesis conditions, the weight fraction of organic material is 0.81. This can be used to estimate a

 SiO_2 nanocore volume fraction of $\phi_c = 0.13$ and a PEG (5 kDa) grafting density $\Sigma \approx 1.6$ chains/nm². Differential scanning calorimetry (DSC) (Q2000, TA Instruments) under nitrogen at a fixed ramp rate of 10 °C/min was used to study thermal transitions of the PEGtethered silica nanoparticles. The sample was first heated to 100 °C, which is above the nominal melting temperature of PEG, to remove any thermal history, and then cooled to −90 °C and heated back to 100 °C. Measurements during the second heating cycle revealed a melting peak at 58.3 °C and a recrystallization peak at 41.2 °C, which remain unchanged in subsequent cycles. The weight fraction crystallinity was estimated to be 58% from the area under the melting peak and the enthalpy of fusion was 92.2 J/g. To determine the effect of DSC temperature scan rate on these transition temperatures, T_m was measured at scan rates ranging from 1 to 20 °C/min, and the results are reported in Figure 2a and summarized in Table S2. From these results, the equilibrium melting temperature and the degree of crystallinity were estimated to be 58.7 °C and 57%, respectively. These values are 5.2 °C and 38% lower than the values obtained when similar measurements are performed using the untethered mPEG-OH (see Figure 2b and Table S2), clearly showing that tethering the polymer to nanoparticles suppresses crystallization.

Small-Angle X-ray Scattering. SAXS measurements were conducted in the D1 station at the Cornell High Energy Synchrotron Source (CHESS). Measurements were performed at temperatures between 75 and 95 °C, that is, above the equilibrium melting temperature of the tethered PEG. Results were also collected for samples annealed under vacuum at 90 °C for 48 h.

The particle scattering intensity $(I_{particle})$ can be written as³⁵

$$I_{\mathrm{particle}} = I_{\mathrm{particle/medium}} - \phi_{\mathrm{medium}} I_{\mathrm{medium}}$$

where $I_{\rm particle/medium}$ is the scattering intensity of the particles in a suspending medium; $I_{\rm medium}$ is the scattering intensity of the suspending medium; and $\phi_{\rm medium}$ is the volume fraction of the suspending medium. For the self-suspended hairy nanoparticles used in this study, the tethered PEG acts as the suspending medium for the silica nanoparticle cores, and the scattering intensity of neat PEG is used as $I_{\rm medium}$ for the hairy nanoparticles. It is known that for a suspension of spherical particles, 25,36

$$I_{\text{particle}}(q) = \phi_c \Delta \rho_e^2 VP(q) S(q)$$

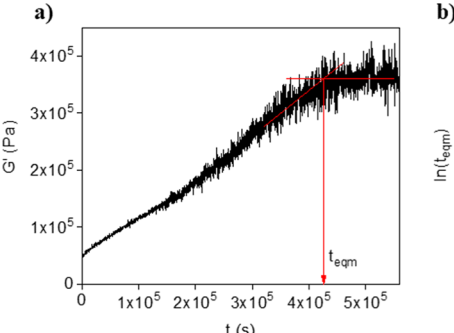
where ϕ_c is the core volume fraction, $\Delta \rho_e$ is the electron density contrast, V is the volume of a single particle core, P(q) is the form factor, and S(q) is the structure factor. In the dilute limit of particle concentration, the interparticle correlations diminish and $S(q) \rightarrow 1$, such that the form factor P(q) can be directly obtained from the scattering intensity. A dilute aqueous suspension of bare charge-stabilized silica nanoparticles (LUDOX SM30) was measured by SAXS for this purpose. The structure factor of the hairy nanoparticles is then obtained by dividing the measured I_{particle} with the form factor P(q) obtained from the dilute suspension. Previous studies show that as temperature increases, the height of the first maximum in S(q) increases, whereas the peak position remains unchanged within instrument resolution, implying more correlated particles with approximately constant interparticle spacing.

Rheological Analysis. Oscillatory and time-dependent shear rheology measurements were conducted using a stress-controlled MCR 501 (Anton Paar) rheometer outfitted with a cone and plate geometry (10 mm diameter, 1° cone angle). Materials used in these studies were rigorously dried at high vacuum overnight before being loaded into the rheometer and were protected in a dry nitrogen atmosphere during measurements. For small amplitude oscillatory shear (SAOS) measurements, frequency sweeps from 0.1 to 100 rad/s were performed at a shear strain $\gamma = 0.5\%$ to study the response of materials in the linear viscoelastic regime. Time sweep measurements for extended amounts of time were performed at a much smaller shear strain $\gamma = 0.01\%$ and at a fixed angular frequency $\omega = 1$ rad/s to monitor how the materials evolve toward equilibrium. To rule out the possibility that the low shear stress in the time sweep affects the

equilibration process, we also performed annealing with no stress for the same amount of time and confirmed that the low shear stress in time sweep had negligible effects on equilibration, as illustrated in Figure S4.3. The SAOS measurements were complemented with large amplitude oscillatory shear (LAOS) analysis at a fixed angular frequency of 1 rad/s and at shear strains γ ranging from 0.01 to 200%. Previous studies of self-suspended hairy nanoparticles show that both the elastic modulus G' and the loss modulus G'' measured in LAOS experiments exhibit plateau values at low strain, comparable to the values measured at intermediate angular frequencies in oscillatory shear experiments. With further increase of the shear strain, the plateau regime is followed by a decay of G', associated with strain softening of the materials, and by the appearance of a distinct maximum in G'', attributed with yielding of soft glassy materials. ^{24,25,27,34} This maximum in G'' is considered the most characteristic of the two material behaviors because it is not observed in entangled polymers and is predicted in simple models in soft glasses to arise from increased viscous dissipation associated with strain-induced cage breakage. ^{38,39} A more complete understanding of these physics is possible from creep and recovery experiments performed on materials deemed equilibrated on the basis of the time sweep analysis. A procedure in which the materials are first presheared in LAOS at a fixed rate $\omega = 1$ rad/s and shear strain $\gamma = 100\%$ for 200 s and then interrogated by imposition of a step stress σ for 1800 s, followed by removal of the stress for another 1800 s. The strain response recorded is reported relative to any residual strain present in the materials at time zero after imposition of the step stress.

RESULTS AND DISCUSSION

Structural Characteristics. Figure 2c,d reports the structure factor S(q) measured in the self-suspended materials before and after annealing. The results show an appreciable change in S(q) before and after annealing. It is known from previous combined experimental and density functional theoretical studies³⁷ that for such materials, the first peak in S(q) reflects the repulsive interactions between the particles, and the second peak arises from the entropic attraction of the cores mediated by the space-filling constraint on the tethered corona polymer chains. The respective peak heights provide qualitative information about the strength of the interparticle correlations. 25,27,37 It is apparent from the results in Figure 2c that the hairy nanoparticles show significant increases in the intensities of both S(q) peaks as temperature rises, with larger increases observed for the annealed material. These trends are quantified in Figure 2d in terms of the temperature-dependent heights of the primary and secondary S(q) peaks deduced from the data in Figure 2c. These results suggest that interparticle interactions generally increase as the temperature rises, for both the unannealed and annealed materials. Such a dependence has been previously observed and is attributed to increased interpenetration of tethered chains. 25,27 The stronger increases in S(q) intensity of the annealed material suggests that both the repulsive and attractive interactions between the particles are enhanced by annealing, possibly reflecting more interdigitated chains and in consequence more correlated particles. The increase in S(0) with annealing is counterintuitive because one would expect the long-wavelength density fluctuation to be suppressed as the interparticle correlation is enhanced. We suspect that the increase in S(0)with annealing might be because the hairy nanoparticles form correlated clusters instead of an ideal uniform lattice. Before annealing, the nanoparticles are less trapped in the clusters they reside in, and thus the long-wavelength density fluctuation is weaker. With annealing, the nanoparticles within their cluster become more equilibrated and thus more correlated, as



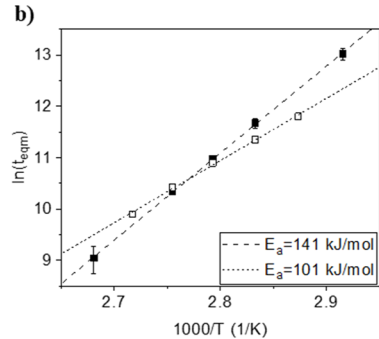


Figure 3. (a) An illustration of small amplitude oscillatory time sweep of the unannealed hairy nanoparticles to monitor in situ the equilibration of the material via storage modulus G'. The time sweep is done at $\gamma = 0.01\%$ and $\omega = 1$ rad/s, and the result shown is measured at 70 °C. An equilibration time ($t_{\rm eqm}$) can be obtained from the extrapolation of the G' curve as shown. (b) Logarithm of equilibration time of the materials vs inverse temperature follows the Arrhenius equation with activation energy $E_{\rm a}$ of 141 and 101 kJ/mol for $\phi_{\rm c} = 0.13$ and $\phi_{\rm c} = 0.22$, respectively.

suggested by the increase in the first peak of S(q). However, the long-wavelength density fluctuation becomes stronger because of the grain boundaries of the equilibrated clusters, which leads to an increase in S(0). The independence of S(0) for the annealed materials with increased temperature that enhances interparticle correlation can be explained with similar rationale. Because SAXS measures the average of scattering of particles at different length scales, we would observe enhanced interparticle correlation upon increase in temperature on the length scale of nanoparticles, as suggested by the first peak height in S(q). However, on a large length scale of the clusters, the long-wavelength density fluctuation is more affected by the grain boundaries of the clusters, which leads to an independence of the more correlated particles within the clusters.

The position of the first peak, q_1 , in S(q) is related to the average interparticle distance, $d_{\rm p-p}$, where $d_{\rm p-p}=2\pi/q_1.^{28}$ As shown in Figure 2c, the position of this peak remains unchanged within experimental resolution for both the unannealed and annealed materials at various temperatures. This indicates that there is no significant change in the interparticle distance upon temperature elevation 25,27 or material annealing, which implies that the enhanced interparticle correlations that increase the magnitude of the S(q) maxima must stem entirely from changes in conformations of the PEG corona chains. From the first peak in S(q), $d_{\rm p-p}$ is estimated to be 17.2 nm, which is in good accordance with the interparticle distance of 17.0 nm estimated from random close packing of spherical particles at the volume fractions estimated from TGA analysis.

Rheological Behavior. To better understand the source of stronger nanoparticle correlations and equilibration of hairy nanoparticle structure associated with annealing, ultra-SAOS (USAOS) measurements ($\gamma = 0.01\%$ and $\omega = 1$ rad/s) were performed in a time sweep mode to monitor how elasticity develops in the materials during the annealing process. The results reported in Figure 3a (see also Supporting Information Figure S4.1) show that over a period of 5.2 days at 70 °C, elasticity develops gradually in the materials and ultimately reaches a plateau value that is approximately 8 times its initial value. The slow increase in G' is consistent with the observation of enhanced particle correlations in S(q), and the attainment of a steady state signifies that the structure of the annealed materials reaches an equilibrium state. This behavior is clearly distinct from aging, which would not lead to

equilibrium and would in fact produce a power-law increase in G^{\prime} at all times. 40,41

The results shown in Figure 3a can be used to deduce both a value for the equilibrium elastic modulus and equilibration time (t_{eqm}) for the materials. Figure 3b reports the equilibration times at various temperatures on a semilogarithmic plot, indicating that $t_{\rm eqm}$ is an exponential decreasing function of temperature. The figure compares t_{eam} versus T for two systems with $\phi_c = 0.13$ and 0.22, respectively. The lines through the data in the figure are best fits to the Arrhenius equation, providing activation energies E_a of approximately 141 and 101 kJ/mol, respectively. Although the Vogel-Fulcher-Tammann-Hesse relationship would approach the Arrhenius equation at temperatures well above the Vogel temperature, due to tethering and jamming of the nanoparticle cores, the long-range cooperative α -relaxation is however considered unlikely. Thus, we consider the fact that t_{eqm} follows the Arrhenius equation as an indication that the slow equilibration process originates from local β -relaxation, rather than α -relaxation of the tethered PEG chains. ^{42–45} The fitted E_a values are compared favorably to activation energies reported for sub- $T_{\rm g}$ segmental motions of various polymers $^{42-47}$ and are significantly larger than the thermal energy available at room temperature (2.5 kJ/mol). Although it is known that the dynamics of tethered chains in hairy nanoparticles is significantly slower than their unconstrained bulk counterparts, 28 this is to our knowledge the first observation that the β -relaxation plays a role in tethered polymer reorientation dynamics at temperatures above the melting transition.

A deeper understanding of polymer dynamics in the cages emerges from an analysis of rheological behaviors of the selfsuspended materials in creep and recovery experiments. Samples were presheared above the yield strain to break down any existing structure and the material response studied at a designated stress to elucidate dynamics associated with cage reconstruction. Typical responses in creep and recovery are shown in Figure 4. At low stresses, the shear strain increases with time, and the material initially appears to flow. The motion dampens as time progresses and is eventually arrested after a certain induction time. As a result, a solidlike, stress-dependent plateau strain, γ_p , is observed at low stresses. We will show later that γ_p is of the same order of magnitude as the apparent yield strain γ_c measured in large amplitude oscillatory strain sweep measurements. At stresses above a critical value between 0.01 and 0.013 MPa, the plateau is no

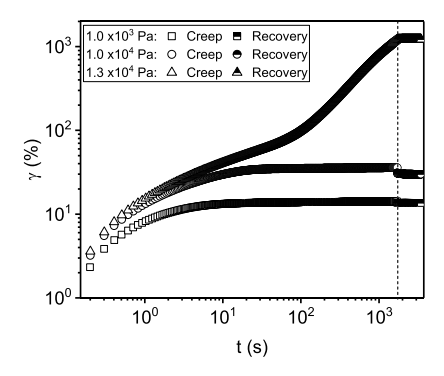


Figure 4. Illustration of creep and recovery tests of the equilibrated hairy nanoparticles following a preshear above the yield strain. The preshear was performed at $\gamma = 100\%$ and $\omega = 1$ rad/s for 200 s. The dotted line indicates the end of the creep test when the stress is removed. The results shown were measured at 70 °C.

longer observed, and the material transitions to a state of continuous flow. Together, these observations suggest that there exists two flow regimes with drastically different dynamics. At small strains, the material exhibits negligible shear modulus and flows slowly in response to an imposed stress. This motion is completely arrested at intermediate shear strains where the effective shear modulus of the material $G_{\rm E} = \sigma/\gamma_{\rm p}$ is higher. At higher stresses, the material appears to break down completely and flows at much higher rates (lower viscosities) than in the low-stress regime. For stresses below the critical value, strain recovery, $\gamma_{\rm R}$, is rapid but incomplete; no strain recovery is observed following the breakdown and flow in the second regime. Consequently, a modulus, $G_{\rm R}$, can be defined from the recovered strain as $G_{\rm R} = \sigma/\gamma_{\rm R}$ only at low-imposed stresses.

As $G_{\rm E}$ is a function of the applied stress and the final strain where flow is arrested, it can provide a measure of the effective

strength of the reformed cages. Results in Figure 5a show that $G_{\rm E}$ is a non-monotonic function of stress and reaches a maximum that decreases with the measurement temperature. Additionally, $G_{\rm E}$ decreases at a critical stress value that also decreases with temperature. Compared to the modulus of equilibrated caging in Figure 3a, the strength of the as-formed caging directly after preshearing above the yield strain in Figure 5a is about an order of magnitude lower. Results in Figure 5c show that $\gamma_{\rm R}$ exhibits a linear relationship with σ over the entire range, indicating that $G_{\rm R}$ is constant. Zooming into the low-stress region, as shown in Figure 5b, we see that at all temperatures, $G_{\rm E}$ is a linear, increasing function of σ . This means that at low stress, the flow is arrested at essentially the same shear strain, regardless of how large a stress is applied.

These behaviors can be explained in terms of microscopic models for the materials, wherein caging only manifests at strains that are large enough to challenge the cage constraint that hairy nanoparticles experience from neighboring particles. At strains below these values, the materials flow in response to an applied stress. The maximum value of $G_{\rm E}$ can therefore be thought of as the maximum strength of the cages, which decreases with the increasing temperature. At even higher σ values, the cages break down and the material flows in response to the imposed stress. At higher temperatures, for example, 90 and 100 °C, $G_{\rm E}$ exhibits a tail after the maximum, which can be attributed to faster cage reconstruction because of faster chain dynamics.

Figure 6a,b reports analogous results from strain-dependent oscillatory shear experiments performed at 75 and 95 °C, respectively. The strain-dependent behaviors, including the appearance of a G'' maximum at an intermediate shear strain, termed the apparent yield strain γ_c has been reported previously. The association of a G'' maximum with yielding has been attributed to the excess viscous dissipation arising from cage breakage and unjamming of soft glassy

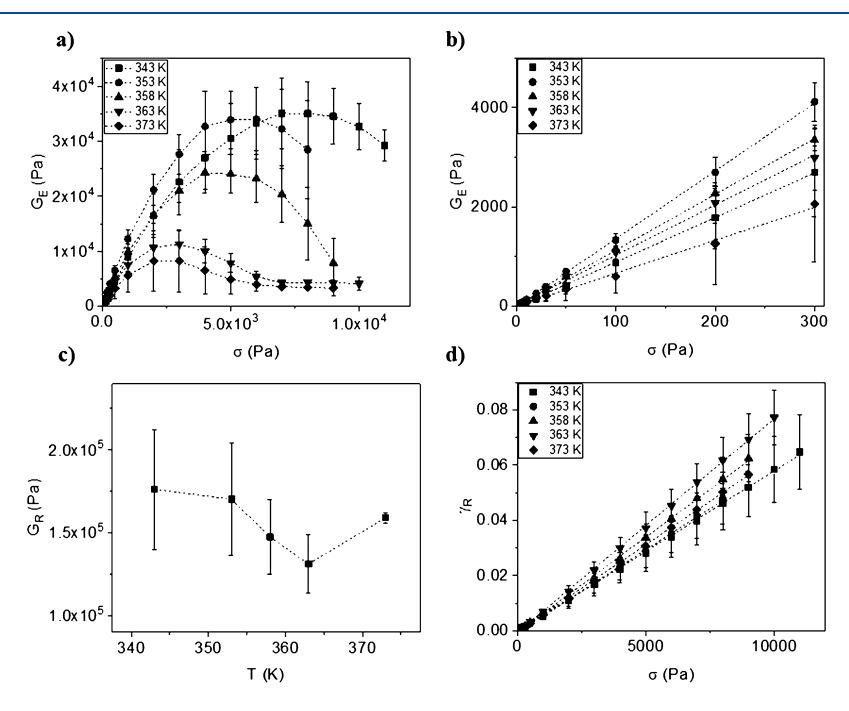


Figure 5. a) Effective modulus (G_E) as a function of stress (σ) applied in creep at various temperatures. (b) G_E as a function of σ at various temperatures shows a linear relationship at low stress. (c) G_R of the equilibrated material as a function of temperature. (d) γ_R as a function of σ at various temperatures shows a linear relationship.

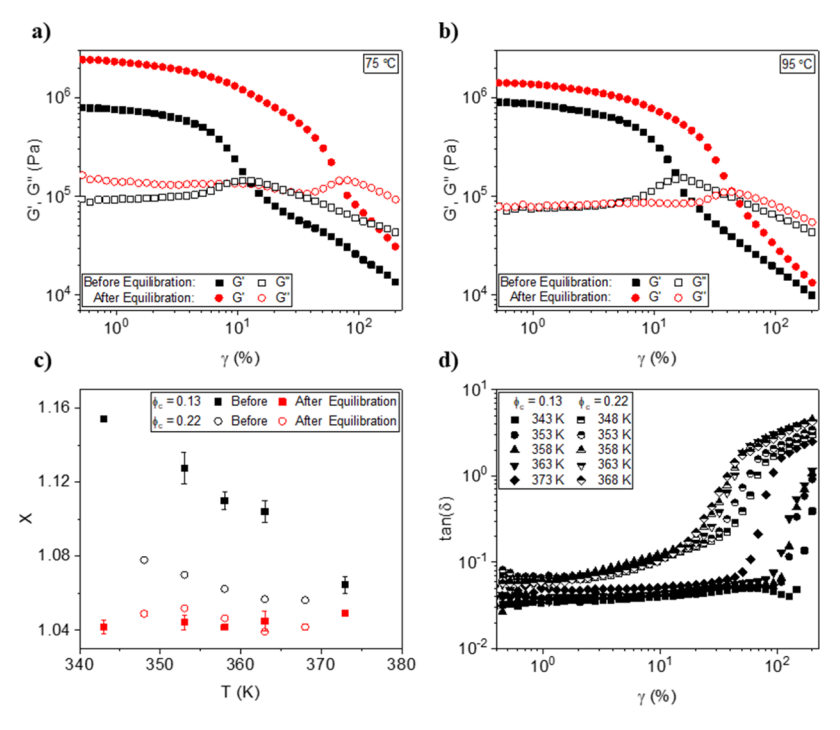


Figure 6. Large amplitude oscillatory strain sweep of the hairy nanoparticles before and after equilibration at 1 rad/s at (a) 75 and (b) 95 °C for ϕ_c = 0.22. (c) Noise temperature, X, of the materials before and after equilibration as a function of temperature. (d) Damping factor $\tan(\delta)$ of the equilibrated materials as a function of strain at various temperatures.

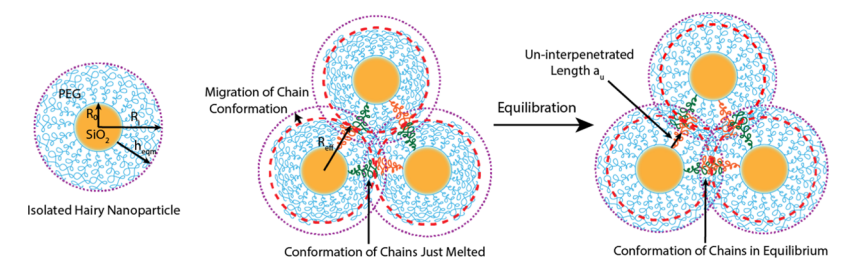


Figure 7. Microscopic illustration of the equilibration of hairy nanoparticles under geometric confinement, where the tethered chains migrate from initially frustrated conformations toward equilibrium conformations upon melting.

materials.^{38,39} At moderate temperature (e.g., 75 °C), annealing produces large enhancements in G' in the linear viscoelastic regime, and the G'' maximum shifts to higher values of strain. Similar effects are apparent at higher measurement temperature (95 °C), but the increase in G' and rightward shift in the G'' maximum are more modest.

The enhancements of G' and G'' and the increased γ_c upon annealing are consistent with the S(q) data, which show that annealing results in increased particle correlations and therefore enhanced caging. The shift in the G'' maximum of the equilibrated materials to larger strain values is more interesting. It argues against the conception that, at a given core volume fraction ϕ_c , the material is more jammed when G'' maximum occurs at lower strains. Shather, it suggests that at a given ϕ_c the cage is strengthened in the equilibrated material and a larger strain is required to pull-out and disengage the interdigitated chains presumed to form the cage.

Figure 6c,d reports the noise temperature, $X = 1 + 2\delta/\pi$, 38,39 and loss tangent $[\tan(\delta) = G''/G']$ deduced from the strain-dependent oscillatory shear rheology. For consistency and accuracy, the δ for the noise temperature calculations is obtained from $\omega = 10$ rad/s in the frequency sweep in the linear viscoelastic regime ($\gamma = 0.5\%$), as shown in Figure S4.4.

Before annealing, the hairy nanoparticles with higher ϕ_c show lower X, implying stronger caging. As the driving force for chain interpenetration that induces caging comes from the space-filling constraint imposed by the interstitial space when packing isolated hairy nanoparticles, for hairy nanoparticles with higher core volume fraction, geometrically the volume ratio of the interstitial space to the polymer corona will increase, which means that the polymer corona will need to stretch more to fill the space, therefore leading to more interpenetration and stronger caging. After equilibration, the materials evidently exhibit more glassy (lower X) behaviors and less temperature-dependent features. The increased glassy behavior is consistent with the increased particle correlations produced by annealing, as observed in the S(q) results. However, the observation that X is a weaker function of temperature for the equilibrated materials than for their unequilibrated counterparts is inconsistent with the notion that increased particle correlations are directly related to enhanced jamming. Rather, it indicates that the material upon equilibration has much less energy available to escape the potential energy wells and is in a considerably more jammed state. The equilibrated hairy nanoparticles exhibit a minor increase in *X* as the temperature increases, implying that more

thermal energy is available to unjam the material, which is in accordance with the weaker cage observed at higher temperature. The materials before the equilibration process show a decreasing X with increasing temperature, suggesting that less energy is available and stronger cages are formed. This is consistent with the strain sweep results before equilibration and likely originates from the larger extent of equilibration achieved in a given amount of loading time at higher temperatures. In Figure 6d, the damping factor $tan(\delta)$ of the equilibrated materials at various temperatures is shown. The upturn of $tan(\delta)$ indicates the breaking of cages, and the shifting of the upturn toward lower strains as temperature increases suggests that weaker cages are formed at higher temperatures. In this regime, the entropic force from a smaller chain deformation is enough to begin the breakdown of the cage structure.

Geometric Analysis of Caging in Self-Suspended Materials. On the basis of the experimental results discussed in the previous sections, we developed a simple geometric model. We begin by considering a hypothetical isolated hairy nanoparticle in the self-suspended materials, where a core of radius R_0 is tethered with polymers that form a corona (Figure 7). Because of the uniform density constraint on corona chains, the thickness of the corona is the average brush height of the tethered chains, originating from the interplay of osmotic pressure and entropic elasticity of the chains. 48 The corona thickness of an isolated particle can therefore be considered as an equilibrium brush height (h_{equil}) of the tethered chains. The uniform density constraint requires the polymer corona to fill the interstitial space associated with packing of isolated particles, which bring the particles closer to each other such that the effective radius of the hairy nanoparticles R_{eff} is smaller than that of an isolated particle R_i . As illustrated in Figure 7, the migration of chains toward equilibrium leads to more interpenetrated chains between particles. As temperature increases, the thermal expansion gives rise to slightly enhanced chain interpenetration, as manifested in the temperature dependence of S(q).

An un-interpenetrated length, $a_{\rm uv}$ can thus be defined as the height of the brush section that is not interpenetrated by chains from an adjacent particle. It provides a length scale where the particles are able to move without disturbing the interpenetrated sections of the chains, which are likely the origin of the cage. Upon equilibrium,

$$a_{\rm u} = d_{\rm p-p} - 2R_0 - h_{\rm eqm}$$

where $d_{\rm p-p}=2R_{\rm eff}$. With the cone-and-plate geometry, the strain γ is uniform everywhere, and the three-particle scheme in Figure 7 can represent any slice of the material system. If we let the top particle move a displacement of Δx relative to the bottom two particles, by definition $\gamma=\Delta x/\Delta y=\Delta x/(\sqrt{3/2}\times d_{\rm p-p})$. Because the interpenetration of the corona is believed to induce caging, we approximate that the top hairy nanoparticle can move without disturbing the caging by a displacement about the un-interpenetrated length $a_{\rm uv}$ that is, $\Delta x \approx a_{\rm uv}$. As $\sqrt{3/2}=0.87\cong 1$, we can thus attain an estimation of yield strain γ_c by

$$\gamma_{\rm c} \cong \frac{a_{\rm u}}{d_{\rm p-p}} \times 100\%$$

Table 2 compares our analytical estimates of γ_c with their experimentally observed analogs of equilibrated materials, with

and without a preshear. As shown in Table 1, the experimentally observed γ_c immediately after equilibration is

Table 1. Comparison of Experimentally Observed γ_c without and with Preshear after Equilibration at Various Temperatures with the Model Predicted γ_c

polymer tethered	$\phi_{ m c}$	γ _c as equilibrated ^a	$\gamma_{\rm c}$ with preshear a	γ_c predicted ^b (%)
PEG (5 kDa)	0.13			12.4
70 °C		$130\%\pm30\%$	$31\%\pm10\%$	
80 °C		$98\% \pm 9\%$	$31\% \pm 3\%$	
85 °C		$99\%\pm20\%$	$32\%\pm5\%$	
90 °C		$90\%\pm20\%$	$31\%\pm7\%$	
100 °C		$56\% \pm 5\%$	$29\% \pm 3\%$	
PEG (5 kDa)	0.22			6.8
75 °C		37.4%	6.0%	
80 °C		27.6%	9.5%	
85 °C		23.7%	8.2%	
90 °C		20.3%	9.5%	
95 °C		20.3%	9.5%	

^aObtained from σ versus γ curve, as shown in Figure S4.2. ^bCalculations are shown in Supporting Information Section 5.

much larger than the theoretically predicted value, whereas the γ_c after a preshear matches the prediction well. The extra strengthening of cages, as evidenced by the larger γ_c , likely comes from chain entanglement, which does not recover instantly after preshear because of the glassy chain dynamics. The reinforced cage hence requires the un-interpenetrated section of the corona to deform more to exert enough entropic force to affect its structure. Without the extra strengthening, as achieved by the preshear, deformation on the length scale of a_n will start to impair the cage structure, which leads to the yielding that agrees with the model. The difference between the experimental and model-predicted γ_c mainly comes from the simplicity of the geometrical model. In particular, it does not take into account the fact that the un-interpenetrated segment is also a coil rather than a stiff string. As a consequence, the un-interpenetrated segment may need to be stretched more to induce enough stress to pull from the interpenetrated region. To the best of our knowledge, Table 2 includes all of the available literature experimental γ_c values for self-suspended hairy nanoparticles that exhibit jamming. Because most of these literature values do not specifically report the γ_c or the shear stress versus strain curve where γ_c can be directly observed, the experimental γ_c values in Table 2 were estimated by the strain in the middle of the G'' upturn in the oscillatory strain sweep, as illustrated in Figure S4.2.

The experimental γ_c values obtained from these reports were deduced following a presehear above the yield strain and should be close to the model predicted γ_c values as has been discussed. The model predicted γ_c values are based on the core volume fraction ϕ_c , which was either directly reported or estimated from the reported core weight fraction or grafting density and tethered chain molecular weight values. It is evident from Table 2 that the model predictions match the experimental results within the same order of magnitude in most of the cases.

The deviation in experimental and predicted γ_c values could arise from discrepancies in the densities of the components used to calculate $\phi_{\mathcal{O}}$ which can affect the results appreciably.

Table 2. Comparison of Experimentally Observed γ_c from the Literature with the Model Predicted γ_c^a

polymer tethered	$\phi_{ m c}$	experimental γ_{c} (%)	γ_c predicted (%)
<u>PI (5 kDa)³⁴</u>	0.10		15.0
−20 °C		20	
0 °C		20	
20 °C		13	
40 °C		10	
60 °C		8	
<u>PI (5 kDa)</u> ³⁰	0.12		13.4
25 °C		10	
<u>PEG (5 kDa)</u> ³⁴	0.122		13.2
70 °C		4	
80 °C		4	
100 °C		5	
120 °C		6	
<u>PEG (2 kDa)</u> ³⁴	0.16		10.5
70 °C		4	
80 °C		4.5	
90 °C		4	
100 °C		4.5	
<u>PEG (5 kDa)</u> ²³	0.162 ^b		10.4
70 °C		3.5	
80 °C		4	
90 °C		6	
100 °C		4	
PS (3.5 kDa) ³⁴	0.17		9.8
130 °C		1.5	
150 °C		3.5	
170 °C		2.5	
190 °C		3	
PBD (3 kDa) ⁴⁹	0.061 ^c		19.9
30 °C		9	
PEG (5 kDa) ²⁷	0.114^{d}		13.8
70 °C		0.25	
80 °C		0.9	
90 °C		1.5	
100 °C		1.5	
135 °C		1.5	
150 °C		0.8	
PEG (5 kDa) ²⁶	0.126 ^e		13.8
90 °C		11	
PEG (5 kDa) ²⁵	0.2		8.0
70 °C		14	
80 °C		14	
100 °C		9	
110 °C	<i>6</i> 11	5.5	

"Core size = 10 nm for all materials examined. "Estimated from 23.5 wt % silica content reported in the original literature. "Estimated from 11 wt % silica content reported in the original literature. "Estimated from 16.97 wt % silica content reported in the original literature. "Estimated from 1.4 chains/nm" reported in the original literature.

For instance, a 2014 study reports the density of silica nanoparticles synthesized by a sol–gel process to be 1.9 g/cm³, which is substantially lower than the densities reported for amorphous silica (2.2 g/cm³) or α -quartz silica (2.65 g/cm³)^{50,51} that previous studies might have used. Additionally, there is no confirmation on whether the materials in the literature have reached the equilibrium state, which could affect the observed ϕ_c . Likewise, errors can originate from the estimation of ϕ_c from the G'' upturn. Considering these

potential sources of discrepancies, there is reasonably a good agreement between our model and the experimental data. Moreover, the model predicts that γ_c will decrease as ϕ_c increases because of the enhanced space-filling effect that leads to deeper chain interpenetration and reduction of a_u . The first six data sets in Table 2 are obtained from the same researcher so that the potential impact of variance in material preparation and inaccurate densities can be ignored when examining the tendency. The γ_c decreases with increasing ϕ_c , which is consistent with the model prediction even if the material systems in these cases are vastly different. It suggests that the interactions that govern the material properties of the self-suspended hairy nanoparticles are largely physical, and the model can be applied as a good starting point for designing hairy nanoparticles with desired properties.

CONCLUSIONS

We investigated slow equilibration dynamics and structural evolution of a soft glassy model system composed of silica nanoparticles covalently tethered with poly(ethylene glycol) chains. The self-suspended hairy nanoparticles exhibit enhanced primary and secondary structure factor peaks during equilibration, indicating that the nanoparticle cores become more correlated, and corona chains are more interpenetrated as the materials equilibrate. SAOS and time sweep rheology measurements reveal a clear transition to a time-invariant, equilibrated state, with characteristic equilibration time that manifests an Arrhenius temperature dependence with an activation energy associated with the β -relaxation of the tethered chains.

Creep and recovery experiments indicate that at shear strains below a certain critical value, there is significant subcage motions in the materials, and that physical properties such as the apparent viscosity deduced from such motions are quite different than those for bulk materials. Creep measurements show further that the strength of the equilibrated cage decreases as the temperature is increased. Transitions in the noise temperature defined using the SGR model confirm the observation that caging is enhanced by equilibration but weakened at elevated temperatures. We interpret the results in terms of time- and temperature enhancement of corona chain interpenetration and, on that basis, propose a simple geometrical model for the materials. The findings reported provide fresh insights into the origin of the caging in selfsuspended hairy nanoparticle fluids that is believed to induce jamming and soft glassy rheology. They also show how dynamics and properties of the cage can be recovered from material response in creep and recovery experiments. Finally, the geometric model proposed to explain the structural and rheological properties of the materials provides a good starting point for understanding the molecular determinants of structure, flow, and thermal behaviors of self-suspended hairy nanoparticle suspensions.

ASSOCIATED CONTENT

Supporting Information

The Supporting Information is available free of charge on the ACS Publications website at DOI: 10.1021/acs.macromol.9b01473.

Thermal gravimetric analysis and calculation of core volume fraction; melting, recrystallization, and crystallinity information of the materials; raw scattering

intensities from temperature-dependent SAXS measurements; storage moduli as a function of time in USAOS rheology; shear stress and loss moduli as a function of strain in oscillatory strain sweep; comparison of quiescent annealing and annealing by USAOS; $\tan(\delta)$ as a function of angular frequency in the linear viscoelastic regime; calculation of yield strain from the geometrical model; and infrared spectroscopy of the materials (PDF)

AUTHOR INFORMATION

Corresponding Author

*E-mail: laa25@cornell.edu.

ORCID ®

Brooks A. Abel: 0000-0002-2288-1975 Lynden A. Archer: 0000-0001-9032-2772

Notes

The authors declare no competing financial interest.

ACKNOWLEDGMENTS

This work was supported by the National Science Foundation, Award no. DMR-1609125. This work is based upon research conducted at the Cornell High Energy Synchrotron Source (CHESS), which is supported by the National Science Foundation under award DMR-1332208. This work made use of the Cornell Center for Materials Research Shared Facilities which are supported through the NSF MRSEC program (DMR-1719875). We also thank Prof. Geoffrey W. Coates for his valuable suggestions and insights on material synthesis.

REFERENCES

- (1) Trappe, V.; Prasad, V.; Cipelletti, L.; Segre, P. N.; Weitz, D. A. Jamming phase diagram for attractive particles. *Nature* **2001**, *411*, 772–775.
- (2) Cates, M. E.; Wittmer, J. P.; Bouchaud, J.-P.; Claudin, P. Jamming, Force Chains, and Fragile Matter. *Phys. Rev. Lett.* **1998**, *81*, 1841–1844
- (3) Srivastava, S.; Agarwal, P.; Archer, L. A. Tethered Nanoparticle-Polymer Composites: Phase Stability and Curvature. *Langmuir* **2012**, 28, 6276–6281.
- (4) Stiakakis, E.; Vlassopoulos, D.; Roovers, J. Thermal Jamming in Colloidal Star—Linear Polymer Mixtures. *Langmuir* **2003**, *19*, 6645—6649.
- (5) Yang, J.; Schweizer, K. S. Tunable dynamic fragility and elasticity in dense suspensions of many-arm-star polymer colloids. *Europhys. Lett.* **2010**, *90*, *66*001.
- (6) Truzzolillo, D.; Vlassopoulos, D.; Gauthier, M. Osmotic Interactions, Rheology, and Arrested Phase Separation of Star–Linear Polymer Mixtures. *Macromolecules* **2011**, *44*, 5043–5052.
- (7) Vlassopoulos, D. Colloidal star polymers: Models for studying dynamically arrested states in soft matter. *J. Polym. Sci., Polym. Phys.* **2004**, 42, 2931–2941.
- (8) Löwen, H.; Watzlawek, M.; Likos, C. N.; Schmidt, M.; Jusufi, A.; Denton, A. R. Phase transitions in colloidal suspensions and star polymer solutions. *J. Phys.: Condens. Matter* **2000**, *12*, A465–A469.
- (9) Helgeson, M. E.; Wagner, N. J.; Vlassopoulos, D. Viscoelasticity and shear melting of colloidal star polymer glasses. *J. Rheol.* **2007**, *S1*, 297–316.
- (10) Scheffold, F.; Cardinaux, F.; Mason, T. G. Linear and nonlinear rheology of dense emulsions across the glass and the jamming regimes. *J. Phys.: Condens. Matter* **2013**, *25*, 502101.
- (11) Denkov, N. D.; Tcholakova, S.; Golemanov, K.; Lips, A. Jamming in Sheared Foams and Emulsions, Explained by Critical

Instability of the Films between Neighboring Bubbles and Drops. *Phys. Rev. Lett.* **2009**, *103*, 118302.

- (12) Zhang, H. P.; Makse, H. A. Jamming transition in emulsions and granular materials. *Phys. Rev. E: Stat., Nonlinear, Soft Matter Phys.* **2005**, 72, 011301.
- (13) Hattori, H. Anti-reflection surface with particle coating deposited by electrostatic attraction. *Adv. Mater.* **2001**, *13*, 51–54.
- (14) Hardikar, V. V.; Matijević, E. Coating of nanosize silver particles with silica. J. Colloid Interface Sci. 2000, 221, 133–136.
- (15) Dabroś, T.; Van De Ven, T. G. M. Kinetics of Coating by Colloidal Particles. *J. Colloid Interface Sci.* 1982, 89, 232–244.
- (16) Mihi, A.; Ocana, M.; Ocaña, H. Oriented colloidal-crystal thin films by spin-coating microspheres dispersed in volatile media. *Adv. Mater.* **2006**, *18*, 2244–2249.
- (17) Ragouilliaux, A.; Ovarlez, G.; Shahidzadeh-Bonn, N.; Herzhaft, B.; Palermo, T.; Coussot, P. Transition from a simple yield-stress fluid to a thixotropic material. *Phys. Rev. E: Stat., Nonlinear, Soft Matter Phys.* **2007**, *76*, 051408.
- (18) Pignon, F.; Magnin, A.; Piau, J. M. Thixotropic colloidal suspensions and flow curves with minimum: Identification of flow regimes and rheometric consequences. *J. Rheol.* **1996**, *40*, 573–587.
- (19) Choi, J. H.; Burns, A. A.; Williams, R. M.; Zhou, Z. X.; Flesken-Nikitin, A.; Zipfel, W. R.; Wiesner, U.; Nikitin, A. Y. Core-shell silica nanoparticles as fluorescent labels for nanomedicine. *J. Biomed. Opt.* **2007**, *12*, 064007.
- (20) Herz, E.; Burns, A.; Lee, S.; Sengupta, P.; Bonner, D.; Ow, H.; Liddell, C.; Baird, B.; Wiesner, U. Fluorescent core-shell silica nanoparticles: An alternative radiative materials platform. *Proceedings of SPIE*, 2006; p 6096.
- (21) Choi, J.; Burns, A. A.; Williams, R. M.; Zhou, Z.; Flesken-Nikitin, A.; Zipfel, W. R.; Wiesner, U.; Nikitin, A. Y. Core-shell silica nanoparticles as fluorescent labels for nanomedicine. *J. Biomed. Opt.* **2007**, *12*, 064007.
- (22) Burns, A.; Ow, H.; Wiesner, U. Fluorescent core-shell silica nanoparticles: towards "Lab on a Particle" architectures for nanobiotechnology. *Chem. Soc. Rev.* **2006**, *35*, 1028–1042.
- (23) Agarwal, P.; Qi, H.; Archer, L. A. The Ages in a Self-Suspended Nanoparticle Liquid. *Nano Lett.* **2010**, *10*, 111–115.
- (24) Agrawal, A.; Wenning, B. M.; Choudhury, S.; Archer, L. A. Interactions, Structure, and Dynamics of Polymer-Tethered Nanoparticle Blends. *Langmuir* **2016**, *32*, 8698–8708.
- (25) Agrawal, A.; Yu, H.-Y.; Sagar, A.; Choudhury, S.; Archer, L. A. Molecular Origins of Temperature-Induced Jamming in Self-Suspended Hairy Nanoparticles. *Macromolecules* **2016**, *49*, 8738–8747.
- (26) Agrawal, A.; Yu, H.-Y.; Srivastava, S.; Choudhury, S.; Narayanan, S.; Archer, L. A. Dynamics and yielding of binary self-suspended nanoparticle fluids. *Soft Matter* **2015**, *11*, 5224–5234.
- (27) Choudhury, S.; Agrawal, A.; Kim, S. A.; Archer, L. A. Self-Suspended Suspensions of Covalently Grafted Hairy Nanoparticles. *Langmuir* **2015**, *31*, 3222–3231.
- (28) Kim, S. A.; Mangal, R.; Archer, L. A. Relaxation Dynamics of Nanoparticle-Tethered Polymer Chains. *Macromolecules* **2015**, 48, 6280–6293.
- (29) Srivastava, S.; Choudhury, S.; Agrawal, A.; Archer, L. A. Self-suspended polymer grafted nanoparticles. *Curr. Opin. Chem. Eng.* **2017**, *16*, 92–101.
- (30) Agarwal, P.; Archer, L. A. Strain-accelerated dynamics of soft colloidal glasses. *Phys. Rev. E: Stat., Nonlinear, Soft Matter Phys.* **2011,** 83. DOI: 10.1103/physreve.83.041402
- (31) Choudhury, S.; Stalin, S.; Deng, Y.; Archer, L. A. Soft Colloidal Glasses as Solid-State Electrolytes. *Chem. Mater.* **2018**, *30*, 5996–6004.
- (32) Choudhury, S.; Vu, D.; Warren, A.; Tikekar, M. D.; Tu, Z.; Archer, L. A. Confining electrodeposition of metals in structured electrolytes. *Proc. Natl. Acad. Sci. U.S.A.* **2018**, *115*, 6620–6625.
- (33) Rodriguez, R.; Herrera, R.; Bourlinos, A. B.; Li, R.; Amassian, A.; Archer, L. A.; Giannelis, E. P. The synthesis and properties of

ı

nanoscale ionic materials. Appl. Organomet. Chem. 2010, 24, 581–589.

- (34) Agarwal, P.; Srivastava, S.; Archer, L. A. Thermal Jamming of a Colloidal Glass. *Phys. Rev. Lett.* **2011**, *107*, 268302.
- (35) Li, T.; Senesi, A. J.; Lee, B. Small Angle X-ray Scattering for Nanoparticle Research. *Chem. Rev.* **2016**, *116*, 11128–11180.
- (36) Glatter, O.; Kratky, O. Small Angle X-ray Scattering; Academic Press: London; New York, 1982; p 515.
- (37) Yu, H.-Y.; Srivastava, S.; Archer, L. A.; Koch, D. L. Structure factor of blends of solvent-free nanoparticle-organic hybrid materials: density-functional theory and small angle X-ray scattering. *Soft Matter* **2014**, *10*, 9120–9135.
- (38) Sollich, P. Rheological constitutive equation for a model of soft glassy materials. *Phys. Rev. E: Stat., Nonlinear, Soft Matter Phys.* **1998**, 58, 738–759.
- (39) Sollich, P.; Lequeux, F.; Hébraud, P.; Cates, M. E. Rheology of Soft Glassy Materials. *Phys. Rev. Lett.* **1997**, *78*, 2020–2023.
- (40) Negi, A. S.; Osuji, C. O. Time-resolved viscoelastic properties during structural arrest and aging of a colloidal glass. *Phys. Rev. E: Stat., Nonlinear, Soft Matter Phys.* **2010**, 82, 031404.
- (41) Gordon, M. B.; Kloxin, C. J.; Wagner, N. J. The rheology and microstructure of an aging thermoreversible colloidal gel. *J. Rheol.* **2017**, *61*, 23–34.
- (42) Iyer, K. A. Chain mobility, secondary relaxation, and oxygen transport in terephthalate copolyesters with rigid and flexible cyclic diols. *Polymer* **2017**, *129*, 117–126.
- (43) Román, F.; Colomer, P.; Calventus, Y.; Hutchinson, J. Study of the Molecular Dynamics of Multiarm Star Polymers with a Poly(ethyleneimine) Core and Poly(lactide) Multiarms. *Materials* **2017**, *10*, 127.
- (44) Konnertz, N.; Böhning, M.; Schönhals, A. Dielectric investigations of nanocomposites based on Matrimid and polyhedral oligomeric phenethyl-silsesquioxanes (POSS). *Polymer* **2016**, *90*, 89–101
- (45) Comer, A. C.; Kalika, D. S.; Rowe, B. W.; Freeman, B. D.; Paul, D. R. Dynamic relaxation characteristics of Matrimid polyimide. *Polymer* **2009**, *50*, 891–897.
- (46) Garwe, F.; Schönhals, A.; Lockwenz, H.; Beiner, M.; Schröter, K.; Donth, E. Influence of Cooperative α Dynamics on Local β Relaxation during the Development of the Dynamic Glass Transition in Poly(n-alkyl methacrylate)s. *Macromolecules* **1996**, 29, 247–253.
- (47) Chowdhury, M.; Freyberg, P.; Ziebert, F.; Yang, A. C.-M.; Steiner, U.; Reiter, G. Segmental relaxations have macroscopic consequences in glassy polymer films. *Phys. Rev. Lett.* **2012**, *109*, 136102.
- (48) Milner, S. T. Polymer Brushes. Science 1991, 251, 905.
- (49) Kim, D.; Srivastava, S.; Narayanan, S.; Archer, L. A. Polymer nanocomposites: polymer and particle dynamics. *Soft Matter* **2012**, *8*, 10813–10818.
- (50) Haynes, W. M. CRC Handbook of Chemistry and Physics; CRC Press, 2014.
- (51) Kimoto, S.; Dick, W. D.; Syedain, Z.; Pui, D. Y.; Roberts, D. L. Effective Density of Silica Nanoparticle Size Standards, 2014 International Aerosol 2014.